

THE OFFICIAL MAGAZINE OF THE OCEANOGRAPHY SOCIETY

Oceanography

CITATION

Alford, M.H., J.B. Mickett, S. Zhang, P. MacCready, Z. Zhao, and J. Newton. 2012. Internal waves on the Washington continental shelf. *Oceanography* 25(2):66–79, <http://dx.doi.org/10.5670/oceanog.2012.43>.

DOI

<http://dx.doi.org/10.5670/oceanog.2012.43>

COPYRIGHT

This article has been published in *Oceanography*, Volume 25, Number 2, a quarterly journal of The Oceanography Society. Copyright 2012 by The Oceanography Society. All rights reserved.

USAGE

Permission is granted to copy this article for use in teaching and research. Republication, systematic reproduction, or collective redistribution of any portion of this article by photocopy machine, reposting, or other means is permitted only with the approval of The Oceanography Society. Send all correspondence to: info@tos.org or The Oceanography Society, PO Box 1931, Rockville, MD 20849-1931, USA.

Internal Waves on the Washington Continental Shelf

BY MATTHEW H. ALFORD, JOHN B. MICKETT,
SHUANG ZHANG, PARKER MACCREADY,
ZHONGXIANG ZHAO, AND JAN NEWTON



TOP | R/V *Thomas G. Thompson* crew and John Mickett of APL/UW preparing Cha Ba for deployment off the Washington Coast. MIDDLE | Field technician Zoë Parsons (UW/APL) and R/V *Thompson* resident technician Justin Smith attach a Wetlabs Water Quality Meter to the mooring wire. BOTTOM | APL/UW deploying Cha Ba from R/V *Robertson* for Puget Sound field tests. *Photos courtesy of Jennifer Hagen, Marine Biologist, Quileute Department of Natural Resources, Quileute Indian Tribe*

ABSTRACT. The low-frequency oceanography of the Washington continental shelf has been studied in great detail over the last several decades owing in part to its high productivity but relatively weak upwelling winds compared to other systems. Interestingly, though many internal wave-resolving measurements have been made, there have been no reports on the region's internal wave climate and the possible feedbacks between internal waves and lower-frequency processes. This paper reports observations over two summers obtained from a new observing system of two moorings and a glider on the Washington continental shelf, with a focus on internal waves and their relationships to lower-frequency currents, stratification, dissolved oxygen, and nutrient distributions. We observe a rich, variable internal wave field that appears to be modulated in part by a coastal jet and its response to the region's frequent wind reversals. The internal wave spectral level at intermediate frequencies is consistent with the model spectrum of Levine (2002) developed for continental shelves. Superimposed on this continuum are (1) a strong but highly temporally variable semidiurnal internal tide field and (2) an energetic field of high-frequency nonlinear internal waves (NLIWs). Mean semidiurnal energy flux is about 80 W m^{-1} to the north-northeast. The onshore direction of the flux and its lack of a strong spring/neap cycle suggest it is at least partly generated remotely. Nonlinear wave amplitudes reach 38 m in 100 m of water, making them among the strongest observed on continental shelves of similar depth. They often occur each 12.4 hours, clearly linking them to the tide. Like the internal tide energy flux, the NLIWs are also directed toward the north-northeast. However, their phasing is not constant with respect to either the baroclinic or barotropic currents, and their amplitude is uncorrelated with either internal-tide energy flux or barotropic tidal forcing, suggesting substantial modulation by the low-frequency currents and stratification.

INTRODUCTION

Internal gravity waves, the undersea analogue to surface gravity waves, are ubiquitous in the world ocean. They cause density layers to move vertically as much as hundreds of meters, with horizontal currents up to a meter per second, in the most active regions such as the South China Sea (Alford et al., 2011). Thought to be primarily generated by the wind blowing on the ocean's surface (leading to "near-inertial waves") and tidal currents flowing over seafloor bumps (leading to "internal tides"), they can give rise to strongly vertically sheared currents and even sweep denser water above lighter water. Both of these instabilities can lead to turbulence and

mixing. As such, they are thought to be major players in mixing both the deep and shallow ocean. In coastal environments, they have the potential to transport nutrients upward into the euphotic zone and transport heat, momentum, nutrients, pollutants, sediment, and even biota such as larvae. However, their slow propagation speed in shallow depths relative to strong low-frequency currents makes them even more variable and complex than in the deep ocean (e.g., see Nash et al., 2012, in this issue).

The Washington continental shelf (Figure 1), at the northern end of the California current system, is a highly biologically productive region that has been the topic of considerable attention of late,

owing to its sensitivity to harmful algal blooms (Horner et al., 1997), hypoxic and anoxic events (Whitney et al., 2008), and ocean acidification (Sabine et al., 2004). A nitrate-limited system, the Washington shelf region appears to be several times more productive than the Oregon or California shelves. Yet, upwelling winds are weaker and more variable than they are further south (Hickey and Banas, 2003). The reasons for this discrepancy have been hypothesized to be related to the presence of the Juan de Fuca Strait, a massive estuary system linking Puget Sound and the Strait of Georgia, the Juan de Fuca eddy, and the Juan de Fuca submarine canyon (Figure 1; Foreman et al., 2008; MacFadyen and Hickey, 2010). In ways that are not yet fully understood, these three unique aspects of the Washington continental shelf may conspire to boost its productivity (Hickey and Banas, 2008).

Internal waves and mixing, are likely key players in these scenarios for Washington waters, though they have not been the subjects of detailed reports. On the New England and Oregon continental shelves, internal waves are responsible for a great deal of the observed mixing, with high-frequency nonlinear internal waves accounting for about half in each case (MacKinnon and Gregg, 2003a; J. Moum, Oregon State University, *pers. comm.*, 2012). In the case of Oregon, turbulence has been observed to enhance the flux of nitrate to the euphotic zone (Avicola et al., 2007). Pineda (1999) demonstrated the potential for nonlinear internal tides to transport invertebrate larvae onto the Southern California continental shelf. Finally, Lucas et al. (2011) inferred lateral nitrate fluxes associated with the internal tide

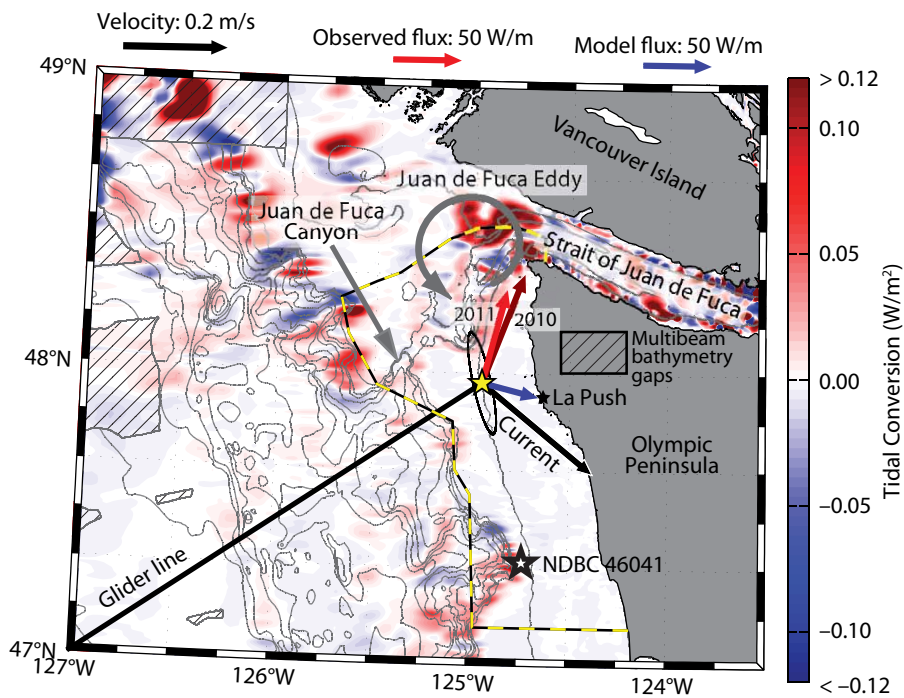


Figure 1. Map showing the location of the Northwest Enhanced Moored Observatory (NEMO) moorings (open star) and glider line (black line), as well as the National Data Buoy Center (NDBC) Cape Elizabeth meteorological buoy 46021 (closed star). Observed barotropic tidal flow and time-mean vector of the current are shown with a dark gray ellipse and arrow, respectively, with scale as indicated. The red and blue arrows are the semidiurnal energy flux computed from observations and model, respectively. The colormap shows conversion of barotropic tidal energy to baroclinic tides (Equation 1). The black and yellow dashed line is the boundary of the Olympic Coast National Marine Sanctuary. Contour levels are each 100 m until 500 m, then each 200 m thereafter.

off California that matched expected nitrate drawdown rates estimated from observed biological production.

We recently designed and deployed a new three-component observing system consisting of two moorings and a glider line off the Washington coast. No turbulence measurements have yet been made. However, the measurements are detailed enough to shed some light on the internal wave field during two successive summers. We observe a rich, variable internal wave field that appears to feature some of the strongest nonlinear internal waves yet reported on continental shelves, when viewed as a fraction of the water depth. This paper is just a first step in presenting these measurements. After first giving a brief primer on internal

waves, we report on the spectral level of the internal waves, the internal tide, and the nonlinear waves on the Washington continental slope. Ongoing work will examine these topics in significantly more detail.

Internal Waves

Anyone who has experimented with a tray of oil atop water has observed internal waves riding on the interface between the fluids. Because the density difference is much smaller than that between the oil and the air above it, the interfacial waves are larger and slower than the “surface” gravity waves above. Moving into the real ocean, where the stratification does not all reside at one interface but is rather continuous, waves

may propagate vertically in addition to horizontally with frequencies up to the buoyancy frequency,

$$N^2 \equiv \frac{-g}{\rho} \frac{\partial \rho}{\partial z},$$

where ρ is the density of seawater. Some interesting properties emerge from solving the linear set of equations for these waves (Lighthill, 1978); for example, group propagation always occurs at right angles to phase propagation. Finally, introducing rotation, the Coriolis or inertial frequency f sets a lower bound on the wave frequency ω such that $f < \omega < N$.

Internal-wave motion tends to be along “characteristic” slopes that are functions of the stratification and the wave frequency. However, the longest vertical scales feel both the sea surface and the seafloor, such that vertical “modes” are appropriate descriptions of the motion. Because vertical displacement is zero at a flat bottom and very small at the surface (rigid lid approximation), a discrete set of modes arises from these boundary conditions. For constant stratification, the modes are sines and cosines. For variable stratification, they must be computed numerically by solving a Sturm-Liouville equation, with the greater stratification typically seen near the surface, leading to shorter vertical scales and greater velocities up shallow, with longer scales and greater vertical displacements down deep. The phase and group speeds can then be computed in straightforward fashion for each mode.

Internal Tides

Energetic peaks in the spectrum of internal waves are typically observed at tidal frequencies. Gravitational forcing by the sun and moon drive large-scale

variations in sea level and predominantly depth-independent (“barotropic”) currents. When the currents associated with this so-called “barotropic tide” flow over seafloor features such as undersea ridges, seamounts, and even the continental slope, baroclinic or “internal” tides (IT) are generated at the same frequency, with nonlinearity leading to higher harmonics or “overtides.” A variety of generation mechanisms exists, depending on the slope of the seafloor relative to the characteristic slope and the lateral excursion of the barotropic tide relative to the scale of the topography (St. Laurent and Garrett, 2002). The energy converted from the barotropic tide to internal tides is

$$C \equiv -p_{bottom} \vec{u}_{BT} \cdot \nabla H, \quad (1)$$

where p_{bottom} is the baroclinic pressure at the seafloor, \vec{u}_{BT} is the barotropic velocity, and H is the water depth (Kelly and Nash, 2010). C can be positive, indicating energy input from the barotropic tide to the internal tide, or negative, indicating the opposite, or barotropic tide gaining energy from the internal tide.

Once generated, waves are seen radiating away from the source along lines of characteristic slope, with the motions transitioning primarily to first and second vertical modes after about a mode-1 wavelength (≈ 150 km in the open ocean). These low-mode internal tides are now known to propagate far, carrying a large fraction (≈ 70 – 80%) of the converted energy thousands of kilometers from the generation regions (Zhao and Alford, 2009). This capacity is partly because their long vertical scales support only very weak shear, and because they interact only slowly with the rest of the internal waves—but also

because the phase speeds of these low modes in the deep ocean are ≈ 3 m s⁻¹, much greater than the low-frequency currents (≈ 0.2 m s⁻¹) that could refract and otherwise disrupt their propagation (Rainville and Pinkel, 2006). This situation contrasts sharply with that on continental shelves, where wave speeds are much slower (≈ 0.4 – 0.5 m s⁻¹) and currents are much faster, so that the two are comparable, allowing much stronger refraction and Doppler shifting of the motions. Additionally, stratification tends to be much more variable near the coasts than in the open ocean, affecting both the generation and propagation of the waves on the shelf.

In addition to these factors affecting internal tides generated near coasts, long-distance-propagating internal tides generated far away can also complicate coastal records, where they appear as “remote” waves that interfere with those generated locally. Complicated and time-variable interference patterns can result (Alford et al., 2006; Martini et al., 2011; recent work of authors Zhao and Alford and colleagues). One useful tool for separating remote and local is by examining the fortnightly spring/neap cycle. Because barotropic forcing typically shows a spring/neap cycle, locally generated baroclinic motions typically do also, with only a short phase lag, given the

proximity to the source. Because ocean signals have propagated far and arise from multiple sources, they tend to be more incoherent, with a less-pronounced spring/neap cycle than local signals. On the other hand, in complex coastal regions such as the Washington continental shelf, barotropic forcing itself can be variable enough to lack a spring/neap cycle, invalidating this approach.

Nonlinear Internal Waves on Continental Shelves

Nonlinear internal waves (NLIWs) are common features of the coastal ocean, often appearing as sharp depressions of the near-surface thermocline with opposing horizontal flow above and below (Apel et al., 1985; Farmer and Armi, 1999; Scotti and Pineda, 2004). They can often be seen in space-borne synthetic aperture radar (SAR) images (Jackson et al., 2012, in this issue). Ostrovsky and Stepanyants (1989) and Apel et al. (2006) give excellent reviews of the topic. NLIWs observed on continental shelves tend to be 10–30 m in amplitude (Table 1), and directed onshore, implying generation at the shelf break. A variety of generation mechanisms are possible (Jackson et al., 2012, in this issue). The many mechanisms that involve tidal flows include lee waves that are formed during one

Matthew H. Alford (malford@apl.washington.edu) is Principal Oceanographer, Applied Physics Laboratory, and Associate Professor, School of Oceanography, University of Washington, Seattle, WA, USA. **John B. Mickett** is Senior Oceanographer, Applied Physics Laboratory, University of Washington, Seattle, WA, USA. **Shuang Zhang** is Research Assistant, Applied Physics Laboratory, School of Oceanography, University of Washington, Seattle, WA, USA. **Parker MacCreedy** is Professor, University of Washington, Seattle, WA, USA. **Zhongxiang Zhao** is Senior Oceanographer, Applied Physics Laboratory, University of Washington, Seattle, WA, USA. **Jan Newton** is Principal Oceanographer, Applied Physics Laboratory, School of Oceanography, University of Washington, Seattle, WA, USA.

phase of the barotropic tide over a bump and then released when the flow relaxes (Maxworthy, 1980; Farmer and Armi, 1999), interaction of internal tide beams with the surface (Pingree and New, 1989), and steepening of internal tides as they shoal (Colosi et al., 2001; Lien et al., 2005; Farmer et al., 2009; Alford et al., 2010). Others involve nontidal flows. One of the most dramatic examples of this type of mechanism occurs when buoyant river plumes enter the much denser ocean interior. As the lateral density gradients evolve, the plumes radiate energetic trains of gravity waves, as observed at the Columbia River mouth, about 200 km to the south of our measurements (Nash and Moum, 2005).

Unlike linear internal waves, which transport momentum and heat but not mass, nonlinear waves have the potential to trap parcels of water within them and carry them appreciable distances (Lamb, 2002; Lien et al., 2012). Because of this property, their potential for transporting nutrients and larvae in coastal

environments has long been appreciated (Sandstrom and Elliott, 1984; Pineda, 1999). They can also transport sediment and pollutants Bogucki et al., 1997; Klymak and Moum, 2003).

The rapid and strong vertical displacements and sheared horizontal flows of NLIWs make them efficient at mixing. Several studies (Sandstrom and Oakey, 1995; Carter and Gregg, 2002; MacKinnon and Gregg, 2003a; St. Laurent et al., 2011; Martini et al., in press) have found substantially elevated turbulence associated with NLIWs, with the first study finding that half of the total turbulence observed over the New England shelf was due to NLIWs. We have not yet measured turbulence on the Washington shelf, but because the waves observed have amplitudes as great as 38 m in 100 m of water—among the largest seen in similar depths—the distinct possibility exists that they could play an active role in the ecosystem’s supply and redistribution of nutrients, plankton, and fish larvae.

DATA AND METHODS

The two moorings, one surface and one subsurface (Figure 1, star), and the glider line (Figure 1, black line), maintained by the University of Washington, are collectively referred to as the Northwest Enhanced Moored Observatory (NEMO); they are part of the Northwest Association of Networked Ocean Observing Systems (NANOOS). The surface mooring, in 100 m of water at 47°57'N, 124°58'W, consists of a UNIX-based buoy controller in a 2 m discus buoy (Figure 2, right), a suite of meteorological sensors, a down-looking 300 kHz acoustic Doppler current profiler (ADCP) to measure full-water-column currents, and instrumentation attached at discrete depths along the main mooring cable to collect a variety of physical, biological, and chemical measurements. Most relevant to the current work are the ADCPs, which sample every five minutes, and Sea-Bird temperature loggers and MicroCAT conductivity-temperature-depth (CTD) sensors at 1,

Table 1. Selected studies of nonlinear waves observed on continental shelves and their amplitudes in relation to water depth.

Location	H (m)	Max. Wave Ampl. (m)	Ratio	Reference
New England Shelf	70	18	0.26	MacKinnon and Gregg (2003a)
	147	30	0.20	Colosi et al. (2001)
New Jersey Shelf	70	15	0.21	Shroyer et al. (2011)
Massachusetts Bay	80	30	0.35	Butman et al. (2006)
Oregon Shelf	80	< 20	< 0.25	J. Moum, OSU, <i>pers. comm.</i> (2012)
Scotia Shelf	80	25	0.31	Sandstrom and Elliott (1984)
	160	50	0.31	Sandstrom and Oakey (1995)
Okhotsk Sea	70	< 20	< 0.29	Nagovitsyn et al. (1991)
South China Sea	400	140	0.35	Lien et al. (2012)
Washington Shelf	100	38	0.38	This study

5, 10, 15, 20, 25, 40, 50, and 60 m depth, which sample every minute. Data are telemetered up the main mooring wire inductively, buffered, archived aboard the buoy controller, and sent back to shore in real time via a Freewave VHF modem. The shoreside modem is mounted atop a communications tower at the US Coast Guard station 13 nautical miles to the east in La Push, WA, and data are transferred back to the University of Washington from there via Internet.

A McLane moored profiler (MP) on a subsurface mooring 500 m to the north of the surface mooring complements the discrete-depth data from the surface mooring, at the expense of time resolution (Figure 2, left). The MP crawls up

and down the subsurface mooring wire at 25 cm s^{-1} between 18 and 92 m depth, completing a profile pair every two hours. Instrumentation includes a Sea-Bird MP52 CTD with a dissolved oxygen sensor, a Falmouth Scientific acoustic current meter, Seapoint fluorometer and turbidity sensors, and a Satlantic Submersible Ultraviolet Nitrate Analyzer (SUNA). The NANOOS MP is the first to carry a nitrate sensor. Data from the subsurface mooring are also telemetered back to shore in real time, via inductive modem to a controller on the subsurface float, to the surface mooring via a small “telebuoy” on an L-tether, and back to the Coast Guard station.

In order to provide spatial context

for the mooring observations, we use results from a realistic ocean circulation hindcast model of the region. The 2006 model simulation, described in detail in Sutherland et al. (2011), has been extensively validated against data on the shelf; however, these comparisons mainly focused on subtidal currents and stratification. The model is forced with realistic wind stress, atmospheric heat flux, rivers, barotropic tides, and subtidal ocean conditions on the open boundaries. Notably, it lacks forcing from any open-ocean internal wave field, so the internal tide it develops is due solely to local barotropic tide interaction with topography. The results of this study, given below, demonstrate that the model significantly

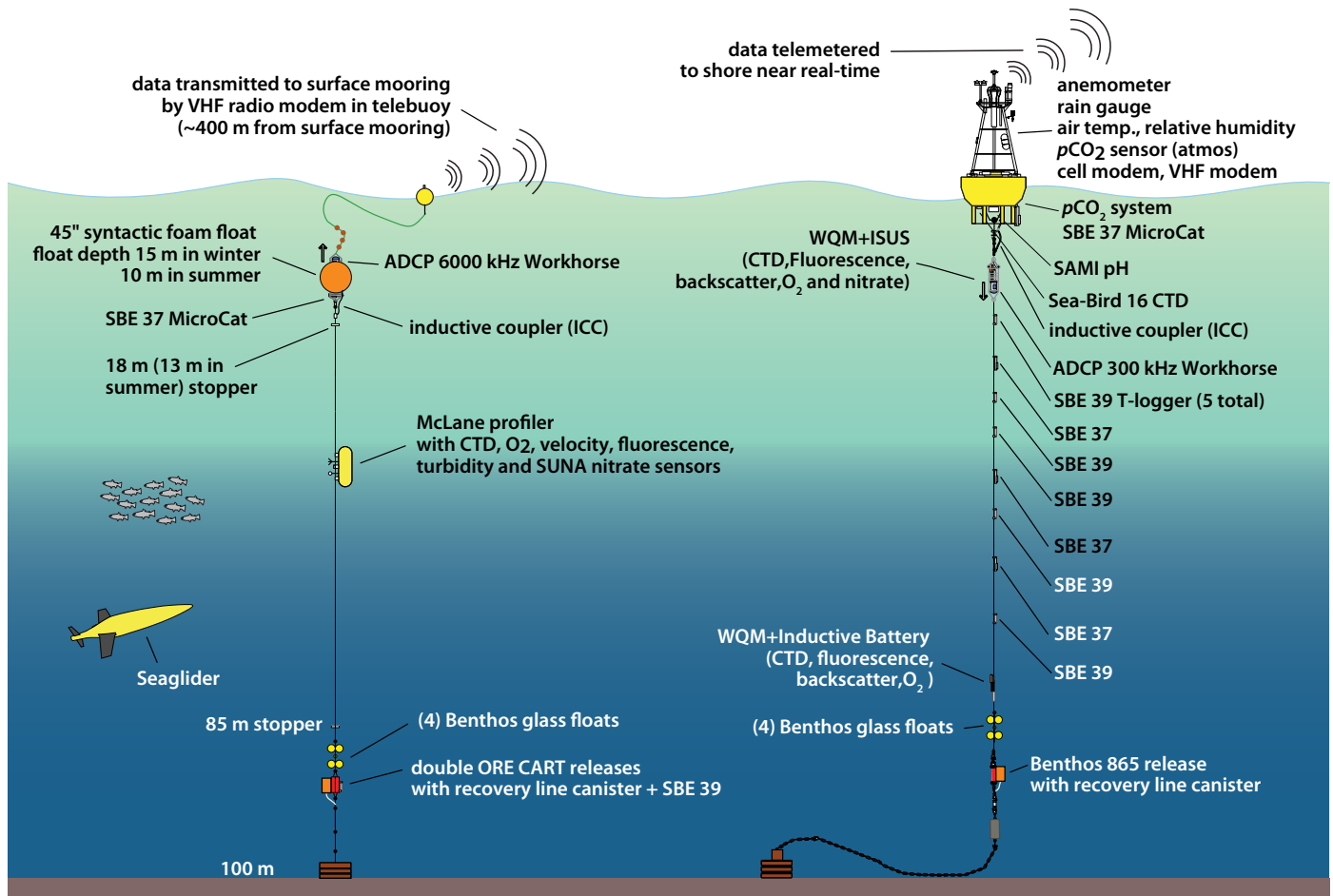


Figure 2. Schematic of the NEMO system showing the surface mooring (right), the subsurface profiling mooring (left), and the glider.

underestimates the observed energy flux of the internal tide at the mooring, suggesting that the neglected internal wave boundary forcing may be important.

The observational systems developed over the past few years will soon be deployed year-round and will be serviced twice yearly as part of the NANOOS program. This paper describes observations from the first two summertime deployments of the system, in 2010 (surface mooring only) and 2011 (both systems), with a focus on the 2011 measurements. The glider data are only used here to provide full-depth stratification information for the flux energy calculations, with the spatial transects deferred for another paper.

OBSERVATIONS

Oceanographic Context

The observed low-frequency currents and stratification are typical of the Washington continental shelf in summer, as described in Hickey (1978) and Hickey and Banas (2003). Winds are predominantly from the northwest (Figure 3a, blue) with periodic southerly winds typically associated with stormy weather (red periods). Currents (Figure 3b) are generally toward the southeast (135° true), as shown by the time-mean vector plotted in black in Figure 1. One to two days following each of the southerly wind events, currents slacken substantially and even reverse at some depths. The depth average current (Figure 3c, green) tends to zero during the most substantial of the wind reversals, but it never quite changes sign. The speed of the low-frequency current varies from ≈ 0 to as great as 0.4 m s^{-1} , the same as the group speed of the fastest internal waves in this water depth and

stratification. It is therefore expected that wave propagation should be affected profoundly as changing currents advect and refract waves.

Figure 4 examines in more detail the 46-day period after August 8 when the subsurface mooring was profiling. Current reversals associated with changes in wind direction are again seen in the velocity plot (Figure 4b). However, at this magnification, the combined semidiurnal barotropic and baroclinic tides appear as regular vertical striations during a 12.4-hour period. The baroclinic tide can be seen as depth-dependent fluctuations in these, and also in the contours of temperature, salinity, and the other scalar fields (Figure 4c–h). Isopycnals (black) demonstrate the vertical motions of the internal tide, which are about 20 m peak-to-peak during the strongest periods.

Temperature, salinity, and stratification generally respond in the expected way to the low-frequency wind shifts, with the upwelling following each wind burst by one to two days, tending to elevate isopycnals and the other scalar fields (e.g., isopycnals rising from August 18–22, then dropping following the downwelling event). The rain gauge on the surface buoy detected 4 cm of rain (not shown) during the August 22 south wind event, which likely also affected shallow stratification.

The semidiurnal fluctuations in velocity and the vertical isopycnal displacement tend to weaken during the periods when the current has weakened (e.g., August 23 and September 19), suggesting a connection between the internal waves and the mesoscale flows that will be examined in more detail in later sections. A natural quantity to

examine is the stratification or buoyancy frequency, N , because it has a direct effect on the vertical scales as well as the generation and propagation speeds of the waves. N (Figure 4e) is clearly modulated at these timescales, though not always in a straightforward way. For example, N increases at the surface during the first two downwelling events, as might be expected, but decreases substantially at depth during the last event, which persists to the end of the record. The complexity is likely at least partly due to three-dimensional effects such as gradients in the along-current/along-shelf direction.

Figure 4f–h presents dissolved oxygen, nitrate, and chlorophyll fields. Because each quantity depends on biological as well as physical processes, they are considerably more complex than the physical quantities. For example, the record begins with high nitrate and low oxygen in the mixed layer, and nearly no observable chlorophyll. A bloom appears on August 13, coincident with the onset of south winds and weakened current, resulting in high chlorophyll. Reduced nitrate and increased oxygen follow, consistent with phytoplankton growth. The internal tide displacements heave the chlorophyll, oxygen, and nitrate fields up and down as the bloom develops. As upwelling resumes, isopycnals are brought upward, but nitrate suddenly increases in the upper 30 m on August 22, implying a lateral transport. Future work will examine the relative roles of the low-frequency currents and the internal waves in modulating these fields.

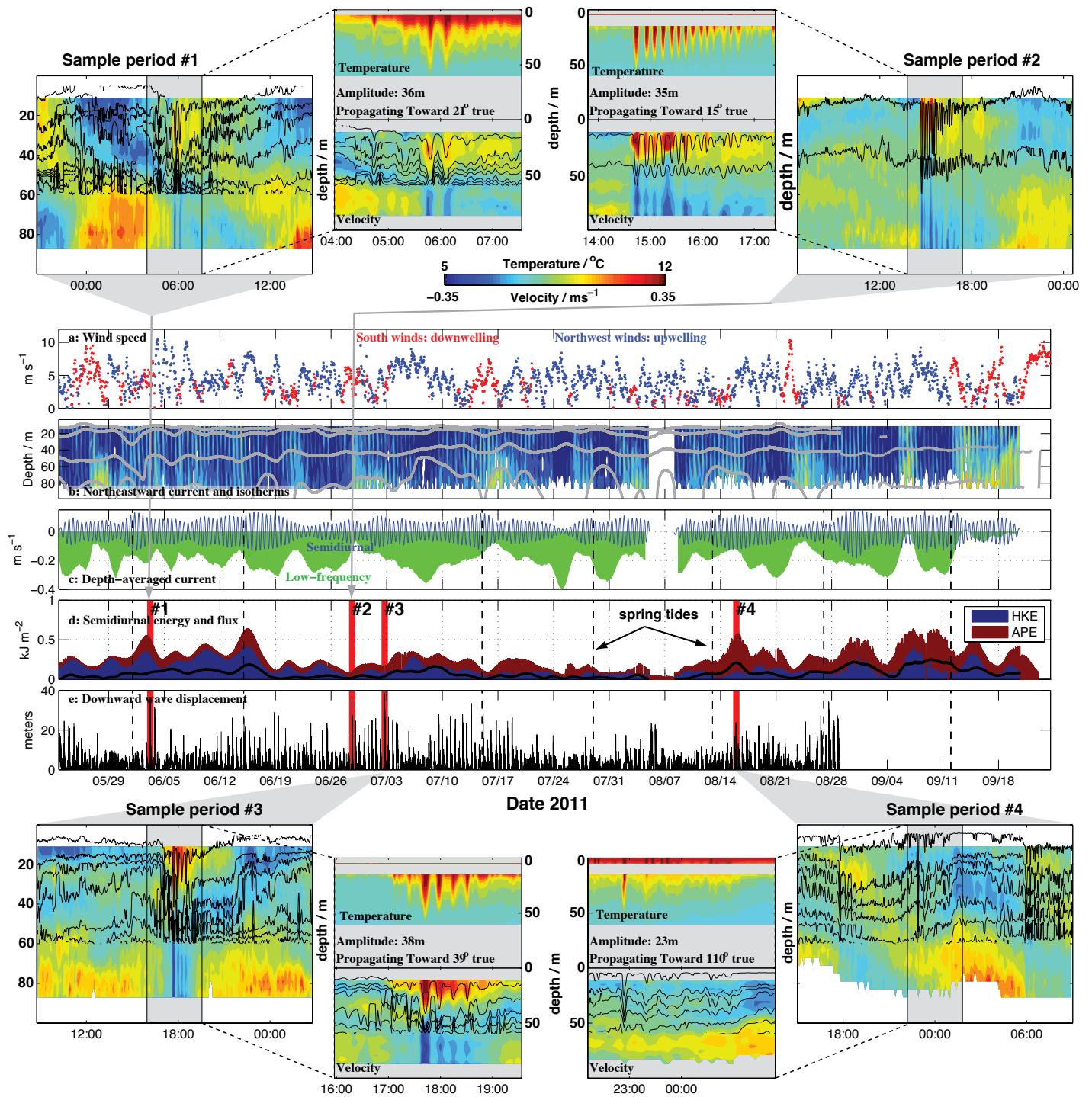


Figure 3. A 2011 time series from the surface mooring, with outer insets showing zoom-ins of 18-hour periods around the four times marked in (d) to demonstrate the variability in the internal tide. Inner insets are zoomed in further on the period indicated in each outer inset to illustrate the temperature (top) and baroclinic northward velocity (bottom) of the nonlinear internal waves. (a) Wind speed, colored by direction (south = red, northwest = blue). (b) Velocity toward 315° true (northwest), with blue colors indicating flow to the southeast. The 8°, 9°, and 10°C isotherms are contoured in gray. (c) Depth-averaged velocity towards 315° true (northwest) of the low-frequency flow (green) and the semidiurnal tidal band (blue). (d) Mode-1 semidiurnal tide: Horizontal kinetic energy (HKE) and available potential energy (APE) are plotted as stacked histograms, with their sum indicating total energy. Energy flux magnitude in kW m^{-1} , which is always toward the north-northeast, is plotted in black. The times of the insets are indicated in red in (d,e). Black dashed lines in (c–e) show full and new moons, which should correspond with spring tides or maximal semidiurnal tidal forcing. (e) Amplitude of the nonlinear internal waves computed by tracking the depth of the isotherm normally at 15 m depth.

Internal Waves

Spectrum

A broad range of frequencies is obvious in both Figures 3 and 4. To quantify the level of the fluctuations at each frequency and compare it to other environments, we compute the spectrum of rotary velocity (Mooers, 1970; Gonella,

1972) using the sine multitaper method of Riedel and Sidorenko (1995). To focus on baroclinic motions, baroclinic velocity \vec{u}_{bc} is first computed by removing the depth mean at each time. By computing the Fourier transform of the time series of $u_{bc} + iv_{bc}$, a frequency spectrum is obtained wherein clockwise

and counterclockwise motions appear at negative and positive frequencies, respectively, which are plotted as blue and green in Figure 5 for 2010 (top) and 2011 (bottom). As expected for internal waves in the Northern Hemisphere, motions are strongly clockwise polarized at frequencies near f , becoming unpolarized by about 10 cycles per day. No prominent near-inertial peak is seen at f , unlike the usual situation in the open ocean. This observation is not surprising given the generally light to moderate winds, because storms are the most efficient generators of near-inertial waves (D'Asaro, 1985). One would expect much stronger near-inertial signals in winter. Instead, semidiurnal and four-times-daily peaks are seen during these summertime records, which are the semidiurnal tide and its "overtide" or first harmonic.

The level of the "continuum" spectrum between f and N gives the strength of the internal wave field, which is thought to be set by nonlinear interactions among the internal waves. In the open ocean, the "GM76" model (Garrett and Munk, 1975, as modified in Cairns and Williams, 1976) provides a framework for comparing continuum levels in different environments. GM76 is over-plotted in gray in Figure 5. For continental shelves, the L02 spectrum (red; Levine, 2002) is more appropriate, because it accounts for the effects of the upper and lower boundaries on the waves, but the two spectral forms are nearly identical for our location. Above the tidal and twice-tidal peaks, the continuum level of the clockwise motions is very close to the L02 and the GM76 model spectra for both 2010 and 2011. At the highest frequencies,

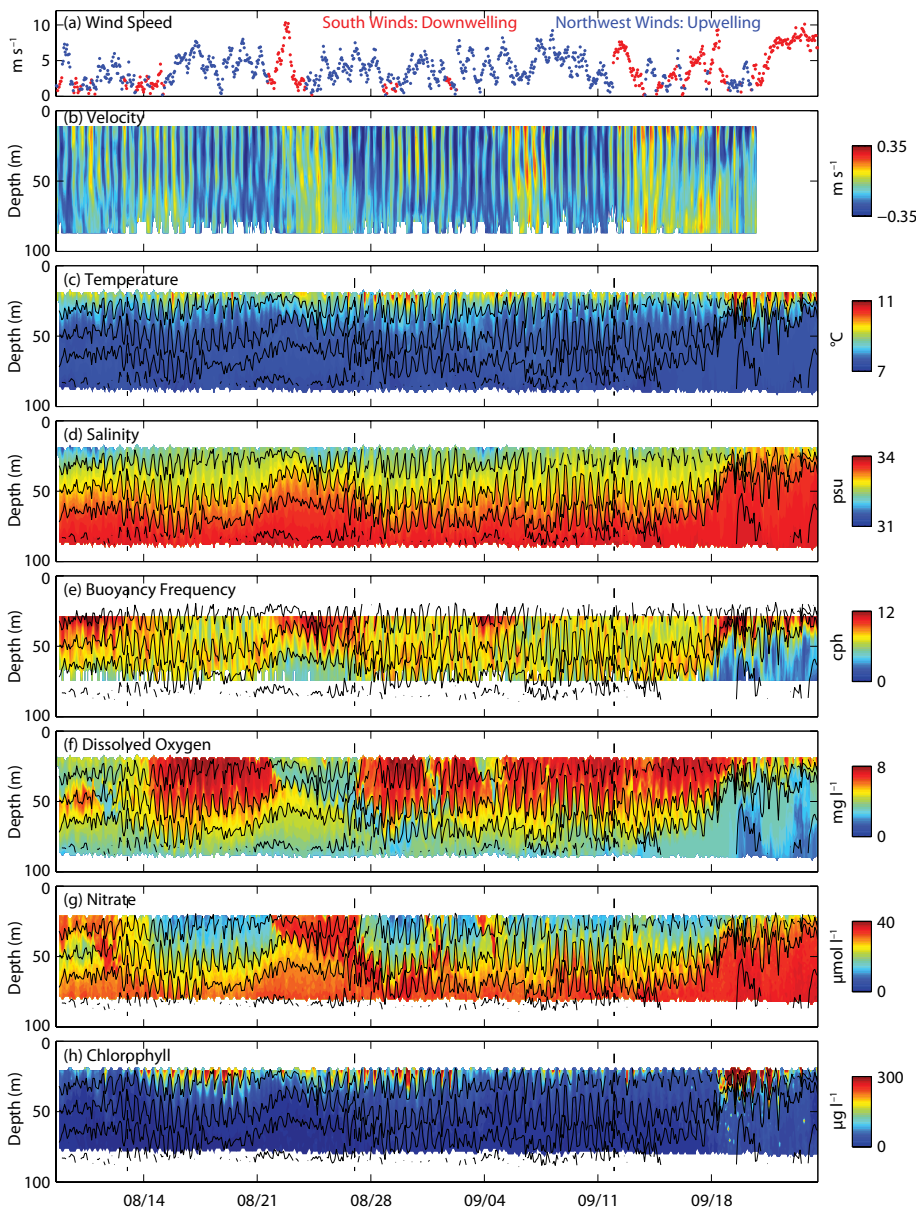


Figure 4. Time series of data from the subsurface mooring, corresponding to the last 46 days of the period plotted in the previous figure. Panels are wind speed colored by (a) direction as in Figure 3, (b) velocity toward 315° true, (c) temperature, (d) salinity, (e) buoyancy frequency, (f) dissolved oxygen, (g) nitrate, and (h) chlorophyll. Isopycnals whose mean spacing is 10 m are over-plotted in each panel in black.

the slope flattens and then drops again, which is the signature of the high-frequency waves so evident in the Figure 3 insets. The rise is well above the noise floor of the instrument, which is below the plotting range at about $7 \times 10^{-7} \text{ m}^2 \text{ s}^{-2} \text{ cpd}^{-1}$. Prior to discussing the high-frequency nonlinear waves, we will next focus on the internal tide and its strength and variability.

Internal Tides

The internal tide contains much of the variance in the velocity spectrum, and so is given special attention in this section. Four periods of the baroclinic velocity record are plotted in close-up in the Figure 3 insets. Each is an 18-hour period, during which the dominance of motions at a ≈ 12 -hour period can be seen. Isotherms measured from the thermistors on the surface mooring are over-plotted in black. Neither velocity nor temperature is filtered, so that the nonlinear waves can be seen (next section). A clear tendency for opposing flow in the upper and lower half of the water column is seen, indicating the dominance of mode-1 motions. Focusing on the tidal-period motions reveals a general tendency for isotherms to be deflected downward during northward flows. This downward deflection of the isotherms is the signature of a wave traveling to the north, because the downward deflection of isopycnals leads to high/low baroclinic pressure in the upper/lower portion of the water column (Althaus et al., 2003). There is, however, considerable variability in the strength of the semidiurnal motions (with the first period showing significantly stronger velocities than the rest), as well as the depth/time structure, with some periods

showing more vertically standing signals, and others (such as the fourth) showing downward phase propagation, implying upward energy propagation.

Quantitative estimates of the energy and energy flux in the internal tide are made following now-standard methods described in Alford (2003), Nash et al. (2005), and Alford and Zhao (2007a). A modal decomposition is first performed to determine the velocity and vertical displacement amplitude associated with each of the vertical modes discussed in the introduction, where the mode shapes are computed using the time-mean stratification taken from the glider profiles near the moorings (acknowledging that temporal changes in stratification can lead to errors, as demonstrated by recent work of authors Zhao and Alford

and colleagues). Baroclinic pressure, p_{bc} , is then computed by integrating the vertical displacement, $\eta(z)$, in depth, assuming motions are hydrostatic (Althaus et al., 2003). The depth-integrated horizontal kinetic energy

$$HKE = \int_{-H}^0 \frac{1}{2} \rho |\bar{u}_{bc}|^2 dz,$$

available potential energy

$$APE = \int_{-H}^0 \frac{1}{2} \rho N^2 \eta^2 dz,$$

and energy flux

$$\bar{F} = \int_{-H}^0 \langle \bar{u}_{bc} p_{bc} \rangle dz,$$

can then be computed. Though semi-diurnal signals dominate, they are nonetheless still isolated via band-pass filtering, using a fourth-order Butterworth filter with cutoffs of 1.7 and 2.3 cycles per day.

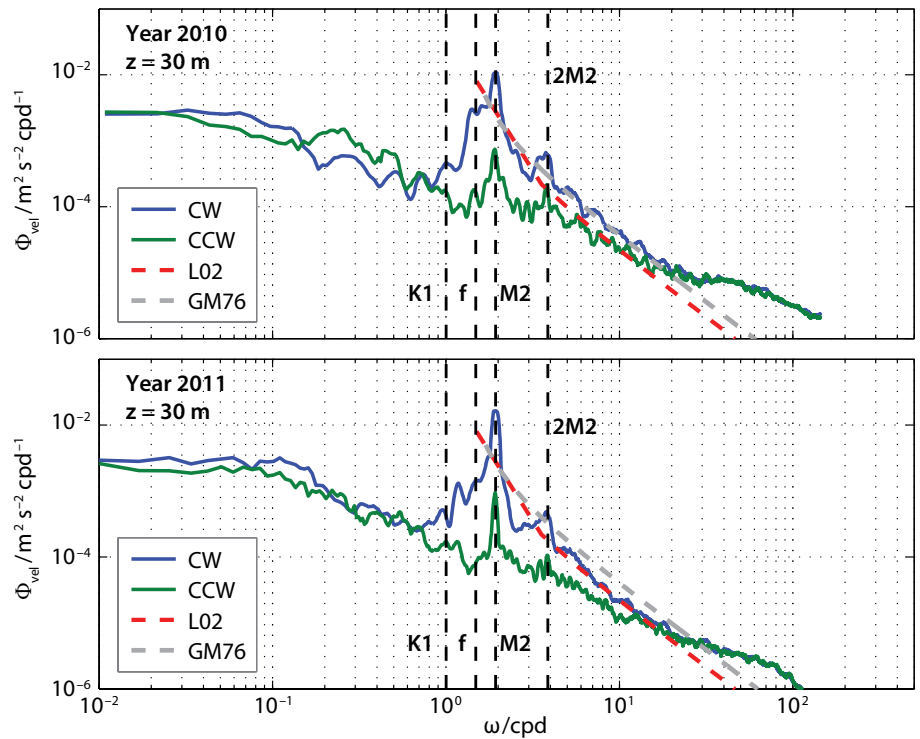


Figure 5. Rotary frequency spectrum of baroclinic velocity at 30 m, measured at the surface mooring during 2010 (top) and 2011 (bottom). The blue and green curves correspond to clockwise and counterclockwise motions, respectively. Vertical dashed lines indicate the near-inertial and tidal frequencies. The Levine (2002) and GM76 model spectra are overlain with red and gray dashed lines, respectively.

These quantities are plotted for the whole period in Figure 3d. As is usual and evident from the insets, the first vertical mode dominates both energy and flux. Mode-1 horizontal kinetic energy (HKE) and available potential energy (APE) are plotted as stacked histograms in red and blue, respectively, with mode-1 energy flux magnitude plotted in black. (Only flux magnitude is plotted because the vector flux is always directed toward the north-northeast.) Energy and energy flux generally rise and fall together, with the ratio near the mode-1 group velocity of 0.4 m s^{-1} , as expected for free waves. However, late in the record, the ratio changes visibly, possibly suggesting interference from waves traveling in different directions (Alford and Zhao, 2007b). Presumably, these changes are due to the different stratification (as observed in recent work of authors Zhao and Alford and colleagues) and/or currents.

As discussed in the introduction, one would expect semidiurnal energy and flux to rise and fall with the barotropic tidal velocity \bar{u}_{BT} , which is estimated as the depth average of the observed semidiurnally band-passed velocity. Semidiurnal barotropic ellipses are about 0.2 m s^{-1} peak-peak and oriented along shelf (Figure 1, gray ellipse), in good agreement with predictions from the TPXO7.2 tidal inverse (Egbert and Erofeeva, 2002). As opposed to the situation in the open ocean, \bar{u}_{BT} (Figure 3c) shows only a weak spring/neap cycle. Maxima generally occur near new and full moons (vertical dashed lines), where the astronomical forcing of the semidiurnal motions is the greatest, but not always (e.g., August 17), indicating the complexity of even barotropic tides in coastal environments.

The baroclinic energy and flux maxima bear little relation to the barotropic forcing, suggesting the presence of remotely incident radiation and/or modulation of the generation and propagation of the local signals by the low-frequency flows. In support of the latter explanation, there is a tendency for flux to be weakest during the periods of weakest northward flow (e.g., July 16, August 23), but the agreement is far from perfect (e.g., September 6). More definitive statements may be possible as the length of the time series grows.

The time-mean semidiurnal energy flux is toward the north-northeast in both years, with magnitudes of 86 and 71 W m^{-1} , respectively (Figure 1, red arrows). These values are similar to those seen on other continental shelves (e.g., 130 W m^{-1} on the New England shelf; MacKinnon and Gregg, 2003b), but much smaller than typical values seen in the open ocean (500 W m^{-1} ; Alford, 2003a) or near strong sources (as great as $6 \times 10^4 \text{ W m}^{-1}$; Alford et al., 2011). As an initial examination of the locally generated internal tide field, conversion (colors) and energy flux (blue arrow) are computed from the numerical model. Because the model has no remotely incident internal tide signals, it is representative of the locally generated internal tides. Though caution must be used in interpreting flux direction in multiple sources owing to the presence of interference patterns, model flux at the mooring location appears to emanate from a region of strong convergence west of Juan de Fuca Canyon. By contrast, the observed fluxes in both years (red arrows) are about twice as large as the model fluxes, and are directed more to the north. The observed fluxes that are

stronger than the modeled ones, their lack of an obvious relationship with the local forcing, and the lack of an obvious conversion region to the south-southeast of the mooring all suggest the fluxes are at least partly of remote origin, possibly from Cape Mendocino (Althaus et al., 2003; Alford, 2010) as observed in Oregon (Martini et al., in press), or even Hawaii (Alford and Zhao, 2007a).

Nonlinear Internal Waves

The 18-hour plots shown in the Figure 3 insets (the four corners) show significant departures from the smooth sinusoids expected for linear waves in both the velocity and temperature signals. To examine these waves in more detail, the 3.5-hour period shown near the center of each plot is replotted in close-up. Sharp waves of depression appear in all four examples as bursts of warm water observed at much greater depth than previously, implying downward displacements of 23–38 m in only 100 m of water. Individual waves last 5–10 minutes and are, therefore, well resolved in temperature, which is sampled every minute. Assuming the waves are propagating at about the mode-1 phase speed for high-frequency waves of 0.5 m s^{-1} , they have horizontal wavelengths of about 150–300 m.

At times, waves occur singly (sample period #4), or in dramatic sets of many waves as in sample period #2. The decrease in amplitude and spacing of the waves following the first is known as “rank ordering,” and follows from the theory for nonlinear internal waves (see Ostrovsky and Stepanyants, 1989). Because larger waves travel faster than smaller waves, they arrive first. The spacing between successive waves decreases

as the waves get smaller and the speed difference lessens. These characteristics are seen in many, but not all, of the waves observed in our data.

The waves show a clear signature in velocity (Figure 3 insets, lower panels), though they are only marginally resolved as velocity is sampled at only five-minute intervals. The baroclinic velocity signature of the waves is mode-1, with each downward displacement accompanied by northward/southward flow in the upper/lower layers. Though only northward velocity is plotted in Figure 3, the measured baroclinic velocity vector in the upper 30 m is used to determine propagation direction (indicated for the four examples in the inset), following Ramp et al. (2004). Direction of these and nearly all waves clusters toward the north-northeast, similar to the direction of semidiurnal flux (Figure 1). The NLIW generation mechanism is as yet unknown, but transformations of shoaling internal tides into internal bores as they transit the shelf break and/or lee-waves generated by barotropic tides flowing past the shelf break are the most likely candidates. The along-shelf orientation of the barotropic tidal ellipses and the propagation of the NLIWs in the same direction as the internal tide are suggestive of the former mechanism, but more work is required to be sure.

The amplitude of the nonlinear waves is computed by tracking the depth of each isotherm relative to a two-day mean, which is intended to represent the slowly varying background state without the displacements of internal waves. The four waves shown in the Figure 3 inset plots range from 23–38 m, in the range of sizes seen on other shelves and continental slopes (Table 1). Expressed

as a fraction of the water depth, the largest waves observed on the Washington continental shelf appear to be among the largest anywhere, exceeding even the amplitude-to-depth ratios seen on the South China Sea continental slope.

Though the waves plotted in the Figure 3 insets are among the largest in the record, the full time series of NLIW amplitude (Figure 3e) shows that waves of 20–25 m are common. The magnitude and frequency of the NLIWs show modulation on a variety of timescales, but appears to bear little relationship with either the barotropic forcing (spring tide times given with dashed lines) or the energy or energy flux of the semidiurnal internal tide (Figure 3d). Waves are at times clearly related to a sharpened front of the downward displacements of the internal tide, as in sample period #1, leading to a sharp decrease/increase in the velocity of the upper/lower layers. However, some waves appear when the internal tide is quite weak, as in sample period #2.

SUMMARY AND DISCUSSION

This paper is the first documentation of internal waves on the Washington continental shelf. The internal wave continuum is close to the model spectrum of L02 for continental shelves (Figure 5). Protruding prominently above this continuum is an active but variable internal tide field (Figure 3, outer insets), and an energetic field of nonlinear waves (Figure 3, inner insets).

The internal tide vertically heaves scalar fields (Figure 4), and propagates toward the north-northeast (Figure 1, red arrows). It appears to be at least partly of remote origin because the observed energy flux is substantially


stronger than in a regional model that includes locally generated tides only. The internal tide is quite variable (Figure 3), displaying neither a clear spring/neap cycle nor an obvious correlation with the local barotropic currents. This observation is some indication that internal tide strength is related to current strength, but more data are required to be sure.

A very energetic NLIW field dominates the high-frequency end of the spectrum. NLIWs on the Washington shelf are among the strongest seen on continental shelves (Table 1). They are clearly related to the internal tide, given that they often occur each 12.4 hours. Like internal tides, NLIWs are directed toward the north-northeast, suggesting that the internal tide possibly generates them via a steepening or related mechanism as described in Colosi et al. (2001) and Lien et al. (2005). On the other hand, their strength and number appear uncorrelated with either the barotropic tidal currents or the energy or flux of the internal tide.

More work is required to determine the origin and generation mechanism of NLIWs. However, their large size makes them potentially important in mixing nutrients upward into the euphotic zone and/or transporting nutrients and larvae laterally on the shelf. Spatial surveys, ideally with microstructure, will be helpful in determining the generation location, propagation pathways, and scalar transport of the waves.

ACKNOWLEDGMENTS

This work was supported in part by the National Oceanic and Atmospheric Administration (NOAA) under IOOS-NANOOS grant NA11NOS0120036 and the National Science Foundation

under grants OCE0968131 (MA) and OCE 0849622 (PM). The considerable hardware and instrumentation comprising the surface and subsurface moorings was purchased on a generous grant from the M.J. Murdock Charitable Trust. Discussions with Barbara Hickey and Neil Banas on the Washington coastal environment and ecosystem were extremely helpful. We are grateful to the captain and crew of R/V *Thomas G. Thompson* for their skill and good attitude in deploying and servicing the moorings. Design and construction of the NEMO system would not have been possible without the hard work and engineering expertise of Eric Boget, Mike Carpenter, Mike Kenney, Trina Litchendorf, Keith Magness, Tim McGinnis, Nick Michel-Hart, Zoë Parsons, Chris Siani, and Tim Wen. We are also indebted to Craig Lee and his group for their assistance in piloting the glider. We are grateful to the Coast Guard station in La Push, Washington, for their hospitality and willingness to host our shore data station and to the Quileute Tribe for their hospitality and access. Finally, we would like to thank the Olympic Coast National Marine Sanctuary for their assistance and cooperation in glider and buoy logistics. 

REFERENCES

- Alford, M.H. 2003. Redistribution of energy available for ocean mixing by long-range propagation of internal waves. *Nature* 423:159–163, <http://dx.doi.org/10.1038/nature01628>.
- Alford, M.H. 2010. Sustained, full-water-column observations of internal waves and mixing near Mendocino Escarpment. *Journal of Physical Oceanography* 40(12):2,643–2,660, <http://dx.doi.org/10.1175/2010JPO4502.1>.
- Alford, M.H., M.C. Gregg, and M.A. Merrifield. 2006. Structure, propagation and mixing of energetic baroclinic tides in Mamala Bay, Oahu, Hawaii. *Journal of Physical Oceanography* 36(6):997–1,018, <http://dx.doi.org/10.1175/JPO2877.1>.
- Alford, M.H., R. Lien, H. Simmons, J.M. Klymak, Y. Yang, D. Tang, and M. Chang. 2010. Speed and evolution of nonlinear internal waves transiting the South China Sea. *Journal of Physical Oceanography* 40(6):1,338–1,355, <http://dx.doi.org/10.1175/2010JPO4388.1>.
- Alford, M.H., J.A. MacKinnon, J.D. Nash, H.L. Simmons, A. Pickering, J.M. Klymak, R. Pinkel, O. Sun, L. Rainville, R. Musgrave, and others. 2011. Energy flux and dissipation in Luzon Strait: Two tales of two ridges. *Journal of Physical Oceanography* 41(11):2,211–2,222, <http://dx.doi.org/10.1175/JPO-D-11-073.1>.
- Alford, M.H., and Z. Zhao. 2007a. Global patterns of low-mode internal-wave propagation. Part I: Energy and energy flux. *Journal of Physical Oceanography* 37(7):1,829–1,848, <http://dx.doi.org/10.1175/JPO3085.1>.
- Alford, M.H., and Z. Zhao. 2007b. Global patterns of low-mode internal-wave propagation. Part II: Group velocity. *Journal of Physical Oceanography* 37(7):1,849–1,858, <http://dx.doi.org/10.1175/JPO3086.1>.
- Althaus, A., E. Kunze, and T. Sanford. 2003. Internal tide radiation from Mendocino Escarpment. *Journal of Physical Oceanography* 33(7):1,510–1,527, [http://dx.doi.org/10.1175/1520-0485\(2003\)033<1510:ITRFME>2.0.CO;2](http://dx.doi.org/10.1175/1520-0485(2003)033<1510:ITRFME>2.0.CO;2).
- Apel, J., L. Ostrovsky, Y. Stepanyants, and J. Lynch. 2006. Internal solitons in the ocean. Woods Hole Oceanographic Institution Technical Report, WHOI-2006-04. Available online at: <http://www.dtic.mil/cgi-bin/GetTRDoc?AD=ADA450369> (accessed May 15, 2012).
- Apel, J.R., J.R. Holbrook, A.K. Liu, and J.J. Tsai. 1985. The Sulu Sea internal soliton experiment. *Journal of Physical Oceanography* 15:1,625–1,651, [http://dx.doi.org/10.1175/1520-0485\(1985\)015<1625:TSSISE>2.0.CO;2](http://dx.doi.org/10.1175/1520-0485(1985)015<1625:TSSISE>2.0.CO;2).
- Avicola, G.S., J.N. Moum, A. Perlin, and M.D. Levine. 2007. Enhanced turbulence due to the superposition of internal gravity waves and a coastal upwelling jet. *Journal of Geophysical Research* 112, C06024, <http://dx.doi.org/10.1029/2006JC003831>.
- Bogucki, D., T. Dickey, and L. Redekopp. 1997. Sediment resuspension and mixing by resonantly generated internal solitary waves. *Journal of Physical Oceanography* 27(7):1,181–1,196, [http://dx.doi.org/10.1175/1520-0485\(1997\)027<1181:SRAMBR>2.0.CO;2](http://dx.doi.org/10.1175/1520-0485(1997)027<1181:SRAMBR>2.0.CO;2).
- Butman, B., P. Alexander, A. Scotti, R. Beardsley, and S. Anderson. 2006. Large internal waves in Massachusetts Bay transport sediments offshore. *Continental Shelf Research* 26:2,029–2,049, <http://dx.doi.org/10.1016/j.csr.2006.07.022>.
- Cairns, J.L., and G.O. Williams. 1976. Internal wave observations from a midwater float, 2. *Journal of Geophysical Research* 81:1,943–1,950, <http://dx.doi.org/10.1029/JC081i012p01943>.
- Carter, G.S., and M.C. Gregg. 2002. Intense, variable mixing near the head of Monterey Submarine Canyon. *Journal of Physical Oceanography* 32:3,145–3,165, [http://dx.doi.org/10.1175/1520-0485\(2002\)032<3145:IVMNTH>2.0.CO;2](http://dx.doi.org/10.1175/1520-0485(2002)032<3145:IVMNTH>2.0.CO;2).
- Colosi, J.A., R.C. Beardsley, J.F. Lynch, G. Gawarkiewicz, C.S. Chiu, and A. Scotti. 2001. Observations of nonlinear internal waves on the outer New England continental shelf during the summer Shelfbreak Primer Study. *Journal of Geophysical Research* 106(C5):9,587–9,601, <http://dx.doi.org/10.1029/2000JC900124>.
- D'Asaro, E. 1985. The energy flux from the wind to near-inertial motions in the mixed layer. *Journal of Physical Oceanography* 15:943–959, [http://dx.doi.org/10.1175/1520-0485\(1985\)015<1043:TEFTTW>2.0.CO;2](http://dx.doi.org/10.1175/1520-0485(1985)015<1043:TEFTTW>2.0.CO;2).
- Egbert, G., and S. Erofeeva. 2002. Efficient inverse modeling of barotropic ocean tides. *Journal of Atmospheric and Oceanic Technology* 19:183–204, [http://dx.doi.org/10.1175/1520-0426\(2002\)019<0183:EIMOBO>2.0.CO;2](http://dx.doi.org/10.1175/1520-0426(2002)019<0183:EIMOBO>2.0.CO;2).
- Farmer, D., and L. Armi. 1999. The generation and trapping of solitary waves over topography. *Science* 283:188–190, <http://dx.doi.org/10.1126/science.283.5399.188>.
- Farmer, D., Q. Li, and J.-H. Park. 2009. Internal wave observations in the South China Sea: The role of rotation and nonlinearity. *Atmosphere-Ocean* 47:267–280, <http://dx.doi.org/10.3137/OC313.2009>.
- Foreman, M., W. Callendar, A. MacFadyen, B. Hickey, R. Thomson, and E. Di Lorenzo. 2008. Modeling the generation of the Juan de Fuca Eddy. *Journal of Geophysical Research* 113, C03006, <http://dx.doi.org/10.1029/2006JC004082>.
- Garrett, C.J.R., and W.H. Munk. 1975. Space-time scales of internal waves: A progress report. *Journal of Geophysical Research* 80(3):291–297, <http://dx.doi.org/10.1029/JC080i003p00291>.
- Gonella, J. 1972. A rotary-component method for analysing meteorological and oceanographic vector time series. *Deep-Sea Research* 19:833–846, [http://dx.doi.org/10.1016/0011-7471\(72\)90002-2](http://dx.doi.org/10.1016/0011-7471(72)90002-2).
- Hickey, B.M. 1978. The California Current System: Hypotheses and facts. *Progress in Oceanography* 8:191–279, [http://dx.doi.org/10.1016/0079-6611\(79\)90002-8](http://dx.doi.org/10.1016/0079-6611(79)90002-8).
- Hickey, B.M., and N.S. Banas. 2003. Oceanography of the US Pacific Northwest coastal ocean and estuaries with application to coastal ecology. *Estuaries* 26(4B):1,010–1,031, <http://dx.doi.org/10.1007/BF02803360>.

- Hickey, B.M., and N.S. Banas. 2008. Why is the northern California Current so productive? *Oceanography* 21(4):90–107, <http://dx.doi.org/10.5670/oceanog.2008.07>.
- Horner, R., D. Garrison, and F. Plumley. 1997. Harmful algal blooms and red tide problems on the US west coast. *Limnology and Oceanography* 42(5):1,076–1,088, http://dx.doi.org/10.4319/lo.1997.42.5_part_2.1076.
- Jackson, C.R., J.C.B. da Silva, and G. Jeans. 2012. The generation of nonlinear internal waves. *Oceanography* 25(2):108–123, <http://dx.doi.org/10.5670/oceanog.2012.46>.
- Kelly, S., and J.D. Nash. 2010. Internal-tide generation and destruction by shoaling internal tides. *Geophysical Research Letters* 37, L23611, <http://dx.doi.org/10.1029/2010GL045598>.
- Klymak, J.M., and J.N. Moum. 2003. Internal solitary waves of elevation advancing on a shoaling shelf. *Geophysical Research Letters* 30(20), 2045, <http://dx.doi.org/10.1029/2003GL017706>.
- Lamb, K. 2002. A numerical investigation of solitary internal waves with trapped cores formed via shoaling. *Journal of Fluid Mechanics* 451:109–144, <http://dx.doi.org/10.1017/S002211200100636X>.
- Levine, M. 2002. A modification of the Garrett-Munk internal wave spectrum. *Journal of Physical Oceanography* 32:3,166–3,181, [http://dx.doi.org/10.1175/1520-0485\(2002\)032<3166:AMOTGM>2.0.CO;2](http://dx.doi.org/10.1175/1520-0485(2002)032<3166:AMOTGM>2.0.CO;2).
- Lien, R., E.A. D'Asaro, F. Henyey, M. Hueti Chang, T.Y. Tang, and Y.-J. Yang. 2012. Trapped core formation within a shoaling nonlinear internal wave. *Journal of Physical Oceanography* 42(4):511–525, <http://dx.doi.org/10.1175/2011JPO4578.1>.
- Lien, R.-C., T.Y. Tang, M.H. Chang, and E.A. D'Asaro. 2005. Energy of nonlinear internal waves in the South China Sea. *Geophysical Research Letters* 32, L05615, <http://dx.doi.org/10.1029/2004GL022012>.
- Lighthill, J. 1978. *Waves in Fluids*. Cambridge University Press, New York, 496 pp.
- Lucas, A., P. Franks, and C. Dupont. 2011. Horizontal internal-tide fluxes support elevated phytoplankton productivity over the inner continental shelf. *Limnology & Oceanography: Fluids & Environments* 1:56–74, <http://lofe.dukejournals.org/content/1/56.full.pdf>.
- MacFadyen, A., and B.M. Hickey. 2010. Generation and evolution of a topographically linked, mesoscale eddy under steady and variable wind-forcing. *Continental Shelf Research* 30(13):1,387–1,402, <http://dx.doi.org/10.1016/j.csr.2010.04.001>.
- MacKinnon, J.A., and M.C. Gregg. 2003a. Mixing on the late-summer New England Shelf: Solibores, shear, and stratification. *Journal of Physical Oceanography* 33:1,476–1,492, [http://dx.doi.org/10.1175/1520-0485\(2003\)033<1476:MOTLNE>2.0.CO;2](http://dx.doi.org/10.1175/1520-0485(2003)033<1476:MOTLNE>2.0.CO;2).
- MacKinnon, J.A., and M.C. Gregg. 2003b. Shear and baroclinic energy flux on the summer New England Shelf. *Journal of Physical Oceanography* 33:1,462–1,475, [http://dx.doi.org/10.1175/1520-0485\(2003\)033<1462:SABEFO>2.0.CO;2](http://dx.doi.org/10.1175/1520-0485(2003)033<1462:SABEFO>2.0.CO;2).
- Martini, K.I., M.H. Alford, S. Kelly, and J.D. Nash. 2011. Observations of internal tides on the Oregon continental slope. *Journal of Physical Oceanography* 41(9):1,772–1,794, <http://dx.doi.org/10.1175/2011JPO4581.1>.
- Martini, K.I., M.H. Alford, S. Kelly, and J.D. Nash. In press. Observations of remotely generated internal tides breaking on the Oregon continental slope. *Journal of Physical Oceanography*.
- Maxworthy, T. 1980. On the formation of nonlinear internal waves from the gravitational collapse of mixed regions in two and three dimensions. *Journal of Fluid Mechanics* 96(1):47–64, <http://dx.doi.org/10.1017/S0022112080002017>.
- Moores, C.N.K. 1970. *The Interaction of an Internal Tide with the Frontal Zone in a Coastal Upwelling Region*. PhD thesis, Oregon State University.
- Nagovitsyn, A., E. Pelinovsky, and Y. Stepanyants. 1991. Observation and analysis of solitary internal waves in the coastal zone of the Sea of Okhotsk. *Journal of Physical Oceanography* 2(1):65–70, <http://dx.doi.org/10.1007/BF02197419>.
- Nash, J.D., M.H. Alford, and E. Kunze. 2005. Estimating internal-wave energy fluxes in the ocean. *Journal of Atmospheric and Oceanic Technology* 22(10):1,551–1,570, <http://dx.doi.org/10.1175/JTECH1784.1>.
- Nash, J.D., and J. Moum. 2005. River plumes as a source of large-amplitude internal waves in the coastal ocean. *Nature* 437:400–403, <http://dx.doi.org/10.1038/nature03936>.
- Nash, J.D., E.L. Shroyer, S.M. Kelly, M.E. Inall, T.F. Duda, M.D. Levine, N.L. Jones, and R.C. Musgrave. 2012. Are any coastal internal tides predictable? *Oceanography* 25(2):80–95, <http://dx.doi.org/10.5670/oceanog.2012.44>.
- Ostrovsky, L.A., and Y. Stepanyants. 1989. Do internal solitons exist in the ocean? *Journal of Geophysical Research* 27:2,906–2,926, <http://dx.doi.org/10.1029/RG027i003p00293>.
- Pineda, J. 1999. Circulation and larval distribution in internal tidal bore warm fronts. *Limnology and Oceanography* 44(6):1,400–1,414, <http://dx.doi.org/10.4319/lo.1999.44.6.1400>.
- Pingree, R.D., and A.L. New. 1989. Downward propagation of internal tide energy into the Bay of Biscay. *Deep-Sea Research Part I* 36(5):735–758, [http://dx.doi.org/10.1016/0198-0149\(89\)90148-9](http://dx.doi.org/10.1016/0198-0149(89)90148-9).
- Rainville, L., and R. Pinkel. 2006. Propagation of low-mode internal waves through the ocean. *Journal of Physical Oceanography* 36:1,220–1,236, <http://dx.doi.org/10.1175/JPO2889.1>.
- Ramp, S.R., D. Tang, T.F. Duda, J.F. Lynch, A.K. Liu, C.S. Chiu, F. Bahr, Y.R. Kim, and Y.J. Yang. 2004. Internal solitons in the north-eastern South China Sea. Part I: Sources and deep water propagation. *IEEE Journal of Oceanic Engineering* 29(4):1,157–1,181, <http://dx.doi.org/10.1109/JOE.2004.840839>.
- Riedel, K.S., and A. Sidorenko. 1995. Minimum bias multiple taper spectral estimation. *IEEE Transactions on Signal Processing* 43(1):188–195, <http://dx.doi.org/10.1109/78.365298>.
- Sabine, C.L., R.A. Feely, N. Gruber, R.M. Key, K. Lee, J.L. Bullister, R. Wanninkhof, C.S. Wong, D.W.R. Wallace, B. Tilbrook, and others. 2004. The oceanic sink for anthropogenic CO₂. *Science* 305:367–371, <http://dx.doi.org/10.1126/science.1097403>.
- Sandstrom, H., and J.A. Elliott. 1984. Internal tide and solitons on the Scotian shelf: A nutrient pump at work. *Journal of Geophysical Research* 89(C4):6,415–6,426, <http://dx.doi.org/10.1029/JC089iC04p06415>.
- Sandstrom, H., and N.S. Oakey. 1995. Dissipation in internal tides and solitary waves. *Journal of Physical Oceanography* 25:604–614, [http://dx.doi.org/10.1175/1520-0485\(1995\)025<0604:DIITAS>2.0.CO;2](http://dx.doi.org/10.1175/1520-0485(1995)025<0604:DIITAS>2.0.CO;2).
- Scotti, A., and J. Pineda. 2004. Observation of very large and steep internal waves of elevation near the Massachusetts coast. *Geophysical Research Letters* 31, L22307, <http://dx.doi.org/10.1029/2004GL021052>.
- Shroyer, E., J. Moum, and J. Nash. 2011. Nonlinear internal waves over New Jersey's continental shelf. *Journal of Geophysical Research* 116, C03022, <http://dx.doi.org/10.1029/2010JC006332>.
- St. Laurent, L., and C. Garrett. 2002. The role of internal tides in mixing the deep ocean. *Journal of Physical Oceanography* 32(10):2,882–2,899, [http://dx.doi.org/10.1175/1520-0485\(2002\)032<2882:TROITI>2.0.CO;2](http://dx.doi.org/10.1175/1520-0485(2002)032<2882:TROITI>2.0.CO;2).
- St. Laurent, L.C., H.L. Simmons, T.Y. Tang, and Y.H. Wang. 2011. Turbulent properties of internal waves in the South China Sea. *Oceanography* 24(4):78–87, <http://dx.doi.org/10.5670/oceanog.2011.96>.
- Sutherland, D.A., P. MacCready, N.S. Banas, and L.F. Smedstad. 2011. A model study of the Salish Sea estuarine circulation. *Journal of Physical Oceanography* 41(6):1,125–1,143, <http://dx.doi.org/10.1175/2011JPO4540.1>.
- Whitney, F.A., H.J. Freeland, and M. Robert. 2008. Persistently declining oxygen levels in the interior waters of the eastern subarctic Pacific. *Progress in Oceanography* 7(2):179–199, <http://dx.doi.org/10.1016/j.pocan.2007.08.007>.
- Zhao, Z., and M.H. Alford. 2009. New altimetric estimates of mode-one M₂ internal tides in the Central North Pacific Ocean. *Journal of Physical Oceanography* 39:1,669–1,684, <http://dx.doi.org/10.1175/2009JPO3922.1>.